





**Response of  $\sim 100$  micron water jets to intense nanosecond laser blasts**Lihao Gao <sup>1,2</sup>, Yanchu Liu <sup>1</sup>, Hui Tang <sup>2,\*</sup> and Weiwei Deng <sup>1,3,†</sup><sup>1</sup>*Department of Mechanics and Aerospace Engineering, Southern University of Science and Technology (SUSTech), Shenzhen 518055, China*<sup>2</sup>*Department of Mechanical Engineering, The Hong Kong Polytechnic University, Hong Kong, China*<sup>3</sup>*SUSTech Center for Complex Flows and Soft Matter Research, Shenzhen 518055, China*

(Received 10 August 2021; accepted 8 February 2022; published 7 March 2022)

We performed an experimental study on water microjets of 100 microns in radius ablated in air by both green (532 nm) and near infrared (1064 nm) nanosecond laser pulses with up to 1100 mJ per pulse. We show this affordable and accessible experimental apparatus captures the essence of the water jet response after being ablated by an intense laser pulse. The results reveal that  $\sim 3.5\%$  of laser pulse energy enters the water jet and half reaches the nozzle orifice as far as 50 times the jet diameter away from the ablation point through internal reflections. The energy density absorbed by the nozzle orifice exceeds the damage threshold of stainless steel, causing microexplosions and formation of a liquid sheet near the nozzle orifice.

DOI: [10.1103/PhysRevFluids.7.034001](https://doi.org/10.1103/PhysRevFluids.7.034001)**I. INTRODUCTION**

The partial destruction of a micro-liquid-jet due to a laser blast is a subject of fundamental importance in physics [1–4]. The intense energy and power flux lead to numerous exciting discoveries and emerging applications [5,6], including nuclear fusion [7], extreme ultraviolet lithography [8], biomacromolecule detections [9,10], and energetic sources of radiation and particles [11]. One prime example is the compact radiation source with short time duration based on relativistically intense laser-plasma interactions [12–14]. These compact facilities are widely applied in a range of application fields such as proton cancer therapy [15] and neutron generation [16]. Liquid jets are rapidly refreshing targets that can operate at much higher repetition rates compared with the solid metal foil targets [17,18]. Study of the laser ablation dynamics of micro-liquid-jets could provide insights on the debris generation and mitigation [19]. Another example is the serial femtosecond crystallography (SFX) based on a liquid jet ablated by an x-ray free electron laser (XFEL) [20]. XFELs have a peak brilliance that is over  $1 \times 10^9$  times brighter than that of synchrotron sources, greatly facilitating the study of weak scattering from small crystals [21,22]. The short XFEL pulse is comparable with the femtosecond-scale chemical time, enabling time-resolved investigation of the reaction dynamics [23]. The XFEL causes a blast that expands against the liquid column in the axial direction, violently breaking the liquid column into two sections [24]. The blast generates a strong shock wave in the water microjet that travels upstream at supersonic speeds [25,26]. The pressure is of particular interest in SFX, as the strong shock raises concern for damage of the jet-delivered protein crystals, which are soft materials held together by weak intermolecular forces [27,28]. SFX involves rich and complex physics that intrigues many scientists. However, the XFEL is a major facility associated with very high construction and maintenance costs; therefore only a handful

\*h.tang@polyu.edu.hk

†dengww@sustech.edu.cn

of XFELs are in operation in the world. The COVID-19 pandemic compounded the complexity of accessing XFEL that often requires international collaborations. On the other hand, the shelf product of a nanosecond pulsed laser is capable of outputting very high power flux that can induce explosion of a liquid jet. For example, a typical commercially available diode pumped  $Q$ -switched pulsed laser can generate a single 10 ns pulse of  $\sim 1$  J on a  $\sim 100 \mu\text{m}^2$  focal point, corresponding to a power flux of  $\sim 10^{18}$  W/m<sup>2</sup>, which is 10 orders of magnitude higher than that of the surface of the Sun. Therefore, the low-cost experimental apparatus of a laser ablated jet allows more engagement of the research community and the results may help complement the study carried out with the actual XFEL. In addition, experimental work in the literature has focused on the short-range energy propagation near the blast center, while the long-range energy propagation that reaches the region near the nozzle orifice has been largely overlooked.

In this work we have performed an experimental study on the water microjet of 100 microns in radius ablated in air by both green (532 nm) and near infrared (1064 nm) nanosecond laser pulses with up to 1100 mJ single pulse energy. With this affordable and accessible experimental system, we recorded and analyzed the complete response of the liquid jet to the laser blast in detail and revealed the mechanism of the liquid response near the nozzle orifice, the results of which provide further understanding of the optical energy propagating mechanism inside microjets. This study shows that, through internal reflections, the laser beam can cause damage to the nozzle tip that is more than 50 times the jet diameter away from the ablation point.

## II. EXPERIMENTAL SETUP

The experimental setup is schematically illustrated in Fig. 1. We used a 1064 nm  $Q$ -switched laser (CNI Laser) with 9 ns pulse duration and adjustable pulse energy up to 1100 mJ. For some experiments, a frequency doubling crystal is installed in front of the laser to convert the 1064 nm wavelength into 532 nm with a maximum pulse energy of 450 mJ. The laser is focused by a planoconvex lens with a focal length of 250 mm and a diameter of 25.4 mm. The laser spot is slightly underfocused with a beam spot diameter of  $\sim 500 \mu\text{m}$  on the jet surface to prevent the laser power density per unit volume from exceeding the ionization threshold of the air. The jet with a diameter of  $160 \mu\text{m}$  is formed by pumping the liquid through a stainless-steel nozzle of  $160 \mu\text{m}$  inner diameter and  $310 \mu\text{m}$  outer diameter at the flow rate of 2.0–3.5 ml/min (corresponds to the jet velocity of 1.5–2.6 m/s and the Weber number of 5–15). To better observe the liquid sheet formed at the nozzle orifice [Figs. 2(a) and 5], we bent the nozzle to an L shape, which allows for the top-view observation. For most of the experiments, the liquid was de-ionized (DI) water, which has a low absorbing coefficient of optical energy of both a 532 and 1064 nm laser; thus the jet acts as a cylindrical lens that further focuses the laser beam to cause a blast near the back surface of the microjet (*front* refers to the side of microjet facing the laser and *back* refers to the opposite side; see Fig. 2). We also performed experiments with water dyed with acid red I (ARI) or rhodamine 6G (R6G) to examine the effects of liquid absorption (ARI) and fluorescence (R6G). The laser energy is fully absorbed within a thin layer of  $\sim 10 \mu\text{m}$  in the 0.025–0.1 wt % ARI-water solution [29]. The R6G solution can be excited by the 532 nm laser and emit 560 nm fluorescence [30]. To visualize the ultrafast laser ablation dynamics, we used a high-speed camera (iX Camera i-Speed 220) coupled with long working distance microscopes with the optical magnification of  $2.25\times$ ,  $5\times$ , and  $10\times$ . The camera has the shortest global shutter time of  $2 \mu\text{s}$ , which is still not short enough to resolve the rapid evolution of the event. To achieve sufficient temporal resolution, we used an in-house-built nanosecond fluorescence flashlight to “freeze” the experimental phenomena (Fig. 1). Because the phenomena are highly repeatable, a time-resolved high-speed photography method was used to achieve a high effective temporal resolution: For each ablation event we imaged multiple shots, each at a variable time delay after the laser pulse. The time delay for the flashlight was varied from  $-1.0$  to  $400 \mu\text{s}$ , and the time interval between two consecutive images was varied from 50 ns to  $10 \mu\text{s}$  according to the speed of the physical process.

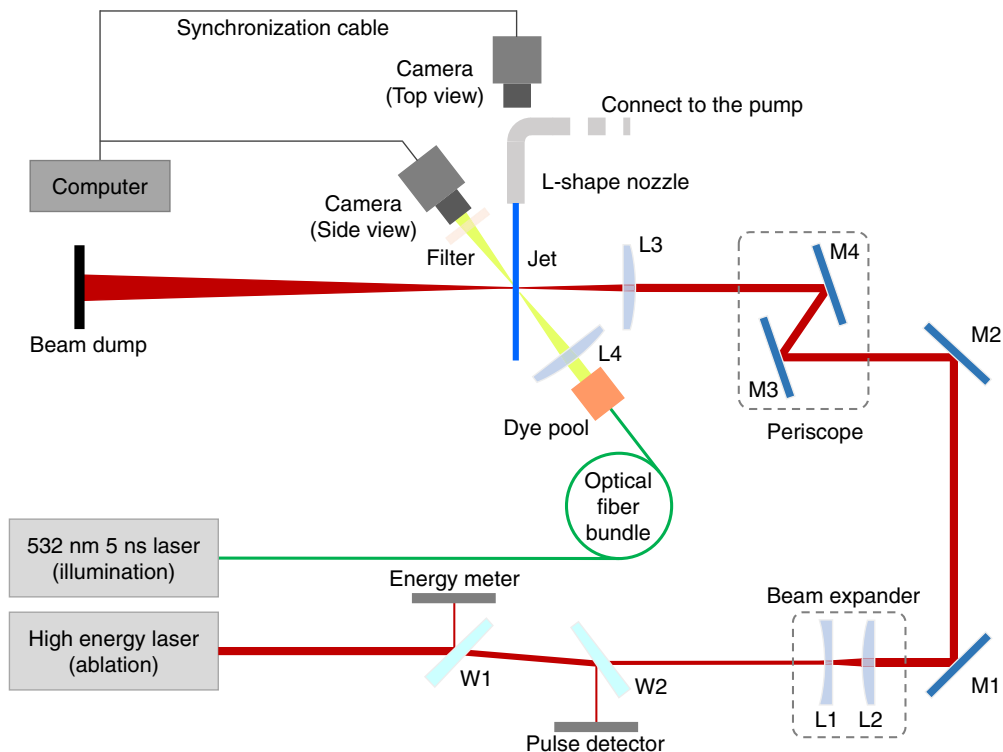


FIG. 1. Schematic of the experimental setup. Microjets are generated from a nozzle driven by compressed air (not shown in this figure), which are ablated by both 532 and 1064 nm high-energy lasers. A laser beam containing about 14% of laser energy is sampled by a wedge (W1), for energy measurement of each pulse by an energy meter; a second laser beam containing about 2% of laser energy is sampled by another wedge (W2, which also eliminates the deviation of the optical beam axis caused by W1), for recording the time delay between each TTL signal and laser pulse. Then the laser beam is expanded by two lenses (L1, L2), reflected by two mirrors (M1, M2) and raised by a periscope structure (M3, M4) before being refocused by a planoconvex lens (L3). The phenomenon is imaged with a time-resolved high-speed photography method, where the illumination is by a 532 nm, 5 ns laser. In order to reduce the coherent speckle, a dye pool filled with rhodamine 6G solution is located behind the optical fiber orifice, which emits 560 nm fluorescence when excited by 532 nm laser. The fluorescence is collected by a lens (L4) for the illumination of the field of view. Long working distance objectives with magnification of  $2.25\times$ ,  $5\times$ , and  $10\times$  are applied in this experiment, and a filter is mounted in front of the objective in order to protect the camera sensor in experiments with 532 nm high-energy laser. The side-view and top-view cameras are synchronized.

### III. RESULTS AND DISCUSSION

#### A. Overall phenomenology

Once the microjet is hit by the laser pulse, bright plasma is generated at the back surface of the microjet [Figs. 2(a)–2(c),  $0 \mu\text{s}$ ], followed by emission of a shock wave into both the surrounding air and liquid columns [Fig. 2(a),  $1.2 \mu\text{s}$ , marked by the red arrow]. The flash gradually decays within  $1\text{--}2 \mu\text{s}$ . Before the flash disappears, a cloud of microdroplets is expelled horizontally towards the incoming direction of the laser pulse [Fig. 2(a),  $1.2 \mu\text{s}$ , marked by the yellow arrow]. This explosion is directional because the DI water jet is transparent to both 532 and 1064 nm lasers so the jet first acts like a cylindrical lens that focuses the laser beam to the back side of the jet, where the plasma appears. A gap appears near the impact point and expands [Fig. 2(a),  $1.2\text{--}140.7 \mu\text{s}$ ]. Meanwhile,

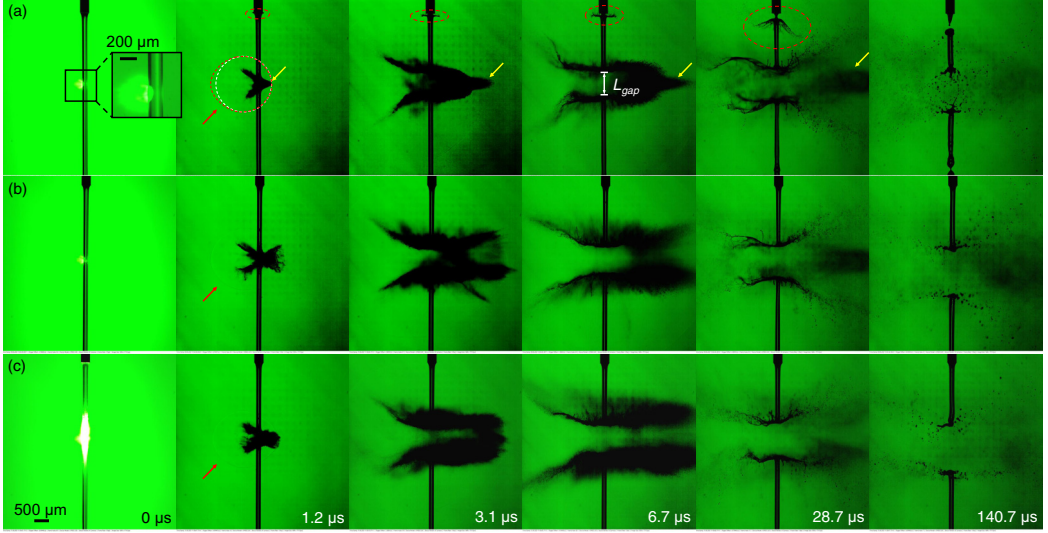


FIG. 2. Temporal evolution near the ablation center. In these images, the laser wavelength is 532 nm, pulse energy is 42–48 mJ, and the direction of all laser pulses is from right to left. The surface of the microjet towards the laser pulse is defined as the *front* surface, while the opposite surface is the *back* surface. (a) The DI water jet. (b) The 0.1 wt% ACI solution jet. (c) The 0.05 wt% R6G solution jet. The red arrow marks the shock wave emitted to the air; the yellow arrow marks the ejected microdroplets; the red dashed line marks the edge of the shock wave; the white dashed line is a standard spherical shape for reference.

the mists keep expanding horizontally, until they finally disappear [Fig. 2(a), 1.2–28.7  $\mu\text{s}$ , yellow arrow]. The liquid column is split into two by the gap and at the end of each column a liquid umbrella forms. The gap grows with time while the liquid sheet expands, bends, and finally breaks up [Fig. 2(a), 1.2–140.7  $\mu\text{s}$ ; also see Fig. 3 for gap expansion]. Increasing the laser pulse energy will result in more violent blasts with brighter plasma flash, faster gap growth, and mist expansion. The basic phenomena (i.e., emission of shock wave, ejection of matter, formation and expansion of the gap, and expansion and retraction of the liquid sheet) remain similar for different laser pulse energies.

Klein and co-workers have pointed out there are four timescales involved in the laser blast of drops [29,31–33]. Similarly, four timescales were also characterized in our research: (i) The duration of the high-energy laser pulse,  $\tau_l \sim 10^{-8}$  s, during which the laser pulse rapidly ionizes and evaporates the liquid to form the explosion; (ii) matter ejection time,  $\tau_e \sim 10^{-6}$  s. In this timescale, a cloud of mist is rapidly ejected (at a speed over 1500 m/s) to the surrounding air; (iii) inertial timescale,  $t_i \sim 10^{-5}$  s, in which the motions (the growth of the gap and the expansion of liquid sheets) are dominated by inertia; (iv) capillary timescale,  $\tau_c \sim (\rho R_j^3/\sigma)^{1/2}$  to  $10^{-4}$  s, where  $R_j$  is the jet radius, and  $\rho$  and  $\sigma$  are the density and surface tension of the liquid, respectively. During  $\tau_c$  the liquid motion is primarily the retraction of liquid sheets, which is dominated by the capillarity. Therefore,

$$\tau_l \ll \tau_e < \tau_i < \tau_c. \quad (1)$$

The expression (1) is very similar to the original relation introduced by Klein *et al.* [29]. However, the characteristic size (i.e., jet radius) in our experiments is  $\sim 80 \mu\text{m}$ , which is one order of magnitude smaller than the drop radius in [29]. The reduction in characteristic length makes the overall process (defined by  $\tau_c$ ) faster in this work than that in [29].

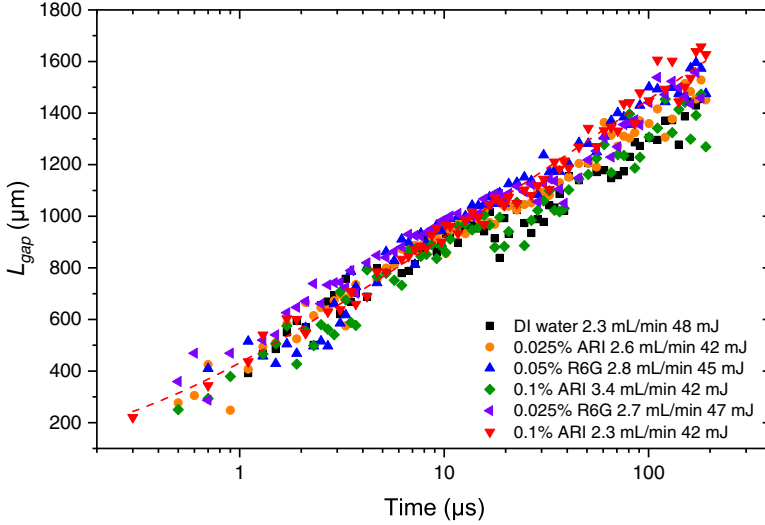


FIG. 3. The logarithmic relation between  $L_{\text{gap}}$  and the time from impact ( $t$ ). Red dashed line shows the fitting result by the logarithmic relation of the experimental data of 0.1% ARI solution, 2.3 ml/min flow rate, and 42 mJ laser pulse energy.

The blast induced gap  $L_{\text{gap}}$  grows with time. Stan and co-workers derived a logarithmic relation between the time and the gap distance based on experiments of the  $20 \mu\text{m}$  jet ablated by femtosecond laser pulse XFEL [24]:

$$\frac{1}{2}L_{\text{gap}} = R_j + CR_j \ln \left( 1 + \frac{t}{\tau} \right), \quad (2)$$

where  $C$  is a numerical constant close to unity and  $\tau$  is a characteristic timescale of the gap growth (which is the ratio of jet radius over the expansion velocity of the cloud after the laser blast). Here we rewrite this relation as  $L_{\text{gap}} \propto \ln(1 + \hat{t})$ , where  $\hat{t}$  is the dimensionless time ( $\hat{t} = 0$  at the beginning of ablation). The gap expansion in our experiments was found to follow this logarithmic relationship (Fig. 3), which is a strong indication that our experiment, although with very different jet diameter as well as laser pulse duration and energy, behaves similarly to that of the jet explosion induced by the femtosecond XFEL laser. This is not surprising because the entire process of laser ablation consists of multiple stages of very different timescales. The gap expansion mainly occurs in the inertial timescale for both  $\sim 10$  and  $\sim 100 \mu\text{m}$  jets; therefore the laser pulse duration is not the governing factor that affects the subsequent gap expansion.

The phenomena are different for liquid jets of ARI solution or R6G solution (see Supplemental Material [34]). Compared to the DI water jet, the left and right sides of the liquid sheet of ARI solution near the gap are more symmetric about the liquid column [Fig. 2(b),  $1.2 \mu\text{s}$ ], which suggests a different mechanism of energy deposition: The laser energy is absorbed along the whole optical path, including both the front and back surfaces. With the R6G solution, the ablation center is very bright, which is the fluorescence that illuminates the jet [Fig. 2(c),  $0 \mu\text{s}$ ].

The most notable difference for the three liquids happens at the nozzle orifice. For the DI water jet blasted by both 532 and 1064 nm lasers, a liquid sheet forms, expands, and finally decays near the nozzle orifice [Fig. 2(a),  $1.2$ – $140.7 \mu\text{s}$ , circled area; also see Fig. 5]. Hundreds of microseconds after the blast, after the liquid sheet disappears, the jet resumes at the nozzle orifice [Fig. 2(a),  $140.7 \mu\text{s}$ ]. For the ARI and R6G solution jets, no such liquid sheet is observed at the nozzle orifice. This suggests that the sheet near the nozzle orifice is not caused by shock waves inside the microjets [25]. A more plausible explanation is that for the DI water jets, part of the laser energy is directed to

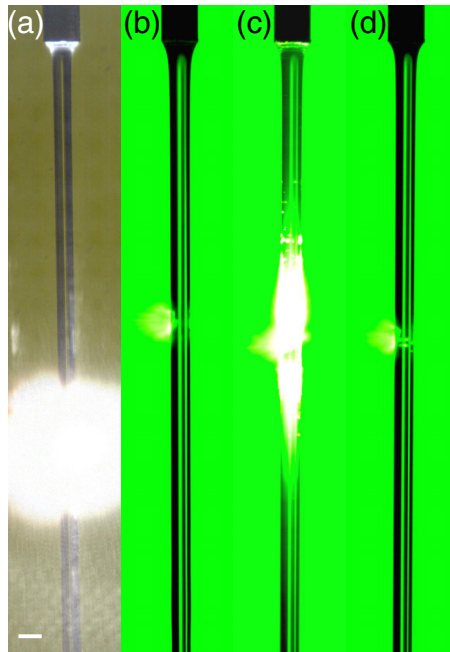


FIG. 4. The flash at  $t = 0 \mu\text{s}$ . (a) DI water jet ablated by 234 mJ, 1064 nm laser pulse. (b) DI water jet ablated by 48 mJ, 532 nm laser pulse. (c) R6G solution jet ablated by 45 mJ, 532 nm laser pulse. (d) ARI solution jet ablated by 42 mJ, 532 nm laser pulse. Scale bar: 200  $\mu\text{m}$ .

the nozzle orifice via scattering of the plasma and subsequent internal reflections in the jet, and the optical energy is deposited near the nozzle tip, causing the phase explosion (a violent, instantaneous boiling due to the localized heating of a thin layer of water, see Sec. III D for details) that expels the water into a sheet. For the DI water jet blasted by the 1064 nm laser pulse, the nozzle orifice is illuminated simultaneously with the bright flash near the blast center [Fig. 4(a)]. Because the 1064 nm laser cannot be observed by either the naked eye or the camera, the illumination in this

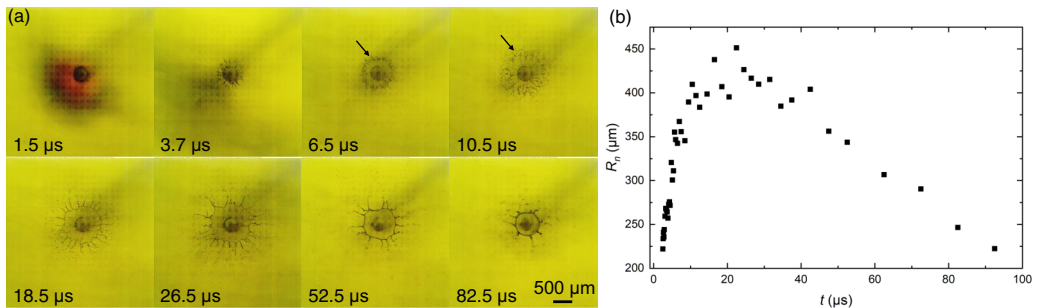


FIG. 5. Liquid sheet evolution at the nozzle orifice after the laser blast. (a) Top-view snapshots of the liquid sheets at  $t = 1.5, 3.7, 6.5, 10.5, 18.5, 26.5, 52.5,$  and  $82.5 \mu\text{s}$ . At  $t = 3.7 \mu\text{s}$ , the fast expanding liquid sheet has a sunflower pattern; at  $t = 6.5$  and  $10.5 \mu\text{s}$ , the shock wave breaks up the rim (marked by the arrow) into a circular cloud of microdroplets; at  $t = 18.5$  and  $26.5 \mu\text{s}$ , during the expansion of the liquid sheet, the rim and ligaments can be clearly observed; at  $t = 52.5$  and  $82.5 \mu\text{s}$ , the liquid sheet shrinks with thicker rim and fewer ligaments. (b) Liquid sheet radius ( $R_n$ ) vs time.

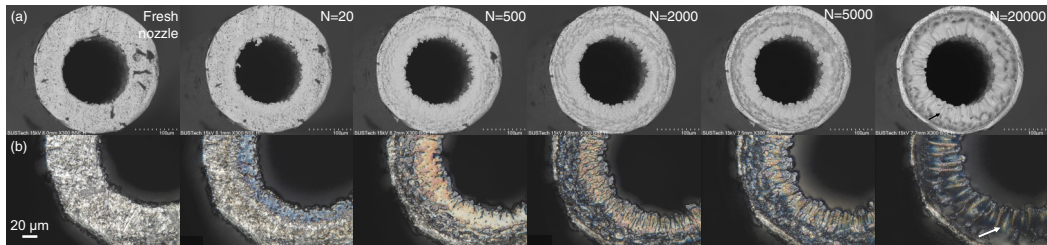


FIG. 6. Damage of the nozzle tip by the laser energy transmitted in the water microjet. (a) SEM images of the nozzle tip and (b) optical micrographs of nozzle tip after 0–20 000 laser pulses. ( $N$ : number of laser pulses).

experiment should come from the intense plasma flash at the ablation point. For the DI water jet blasted by the 532 nm laser pulse, the refracted laser illuminated the entire jet and might have damaged the camera sensor in our experiments. Thus, we reduced the pulse energy from  $\sim 200$  to  $\sim 40$  mJ and added a bandpass filter that only allowed the light of a wavelength of  $565 \pm 24$  nm (i.e., the wavelength of the stroboscopic light source) to pass through, ensuring that the 532 nm laser was blocked. For the rhodamine 6G dyed water jet, the fluorescence can pass the filter and two illuminated regions (the laser ablation point and the nozzle orifice) are visible again [Figs. 4(b) and 4(c)]. These phenomena suggest that photons from both the plasma flash and laser beam can be transmitted inside the jet to the nozzle orifice through internal reflections. However, the primary optical irradiation from the laser and the secondary optical emission from the plasma contribute differently to the phenomenon near the nozzle orifice (also see Sec. III D).

### B. Liquid sheet evolution at the nozzle orifice

When the liquid is transparent to the laser, the blast produces a liquid sheet at the nozzle orifice that first expands and then retracts [Fig. 5(a)]. The liquid sheet has a rim and sunflower pattern near the edge. The inner region of the liquid sheet has several radial wrinkles. The liquid sheet first expands quickly with a maximum velocity over 100 m/s. After time  $\tau_b$  (the time required for the shock wave to travel from the blast center to the nozzle orifice, which ranges from 5 to 10  $\mu$ s in most of our experiments) the shock wave reaches the liquid sheet and breaks the rim into a circular cloud of microdroplets [Fig. 5(a), 6.5–10.5  $\mu$ s; also see Fig. 2(a), 3.1–6.7  $\mu$ s].  $\tau_b$  depends on the distance between laser beam and nozzle orifice and has a magnitude of  $\sim 10$   $\mu$ s in our experiments. After the shock wave passes the liquid sheet, a refreshed rim forms and continues to expand for tens of microseconds, until a maximum radius is reached. After that, the liquid sheet retracts in the next  $\sim 100$   $\mu$ s until it merges with the liquid column.

We estimated the characteristic thickness of the liquid sheet,  $h$ , by the Taylor-Culick speed of a retracing liquid film:  $h = 2\sigma/\rho v^2$ , where  $v$  is the sheet retracing speed, and  $\sigma$  and  $\rho$  are the surface tension and density of the liquid, respectively. This gives  $h = \sim 15$   $\mu$ m in the experiment shown by Fig. 5(b). Here we assume constant surface tension that is not affected by the localized heating on the liquid-nozzle interface (see Sec. III D for detail), because the thermal diffusion length of water is only  $\sim 1$   $\mu$ m.

### C. Nozzle tip damage

We observed the nozzle tip after the microjet experienced multiple laser blasts. Figure 6 shows the scanning electron microscope (SEM) and optical micrographs of the same nozzle tip after increasing the number of laser blasts ( $N$ ) to the liquid jet. We found that the nozzle tip starts to show signs of damage after only 20 blasts [Figs. 6(a) and 6(b),  $N = 20$ ], forming a blue-colored annular area. More blasts cause an expanded damaged area and the color turns gray or orange [Figs. 6(a) and 6(b),  $N = 500$ ]. The increase in the radius of the damaged area mostly occurs within the first

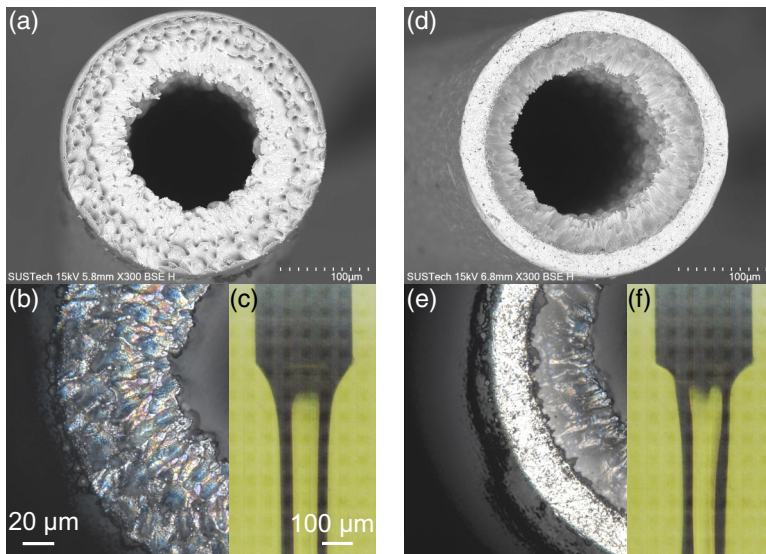


FIG. 7. The nozzle damage patterns after same laser blasts ( $N = 8000$ ) at different flow rates. (a) SEM and (b) optical microscope observation of the nozzle tip with a flow rate of 2.21 ml/min; (c) a snapshot of the nozzle and jet; (d) SEM and (e) optical microscope observation of the nozzle tip with a flow rate of 7.97 ml/min; (f) a snapshot of the nozzle and jet.

1000 pulses. After that, more pulses will mainly deepen the damaged zone rather than enlarge it, exhibiting a layered damage structure [Figs. 6(a) and 6(b),  $N = 2000, 5000$ , and 20 000]. Crystalline grains of the stainless steel can be observed after 2000 laser pulses. The damaged zone turns from coarse column grains [Figs. 6(a) and 6(b),  $N = 2000$ ] to fine grains [Figs. 6(a) and 6(b),  $N = 5000$  and 20 000]. After 10 000 pulses, radial wrinkles (marked by arrows in Fig. 6) are observed. This wrinkled structure with grooves may be what causes the sunflower pattern of the liquid sheet near the nozzle orifice [Fig. 5(a)].

The damaged pattern is also influenced by the shape of the liquid meniscus connecting the nozzle and the jet. The meniscus of different curvature affects the internal reflection of optical beams. Figure 7 shows two damaged nozzle tips, where the only difference is the velocity of the microjet and the associated meniscus curvatures. With a lower jet velocity (1.7 m/s), the radius of curvature of the meniscus is greater, which results in the damage of the whole nozzle tip [Figs. 7(a) and 7(c)]. For a much higher jet velocity of 6.0 m/s, the radius of curvature decreases, and the damaged area of the nozzle tip is confined to the inner half along the radial direction [Figs. 7(d)–7(f)].

#### D. Optical power transmission within the liquid jet

To investigate the mechanism of optical power transmission within the jet, we designed an experiment [Fig. 8(a)] for direct measurement. We made the liquid jet impinge directly on a sealed optical window before the jet breaks up, below which the optical sensor (Thorlabs PDA36A2 for power or Thorlabs ES220C for energy) is positioned to measure the optical power or energy transmitted downstream. An aperture that blocks the unwanted scattered light from the ambient is attached to the optical window. Assuming equal optical power transmission upstream and downstream, the measured optical power is also the value reaching the nozzle orifice. We define the coupling efficiency as the ratio of transmitted power  $p_t$  (cw laser) or energy  $E_t$  (pulsed laser) to injected power  $p_0$  or energy  $E_0$ , i.e.,  $\eta = p_t/p_0$  (for a cw laser) or  $\eta = E_t/E_0$  (for a pulsed laser).

We found that for the same liquid jet and same intercepting point, the cw laser and pulsed laser lead to dramatically different coupling efficiencies. When a 928 mW, 520 nm cw laser



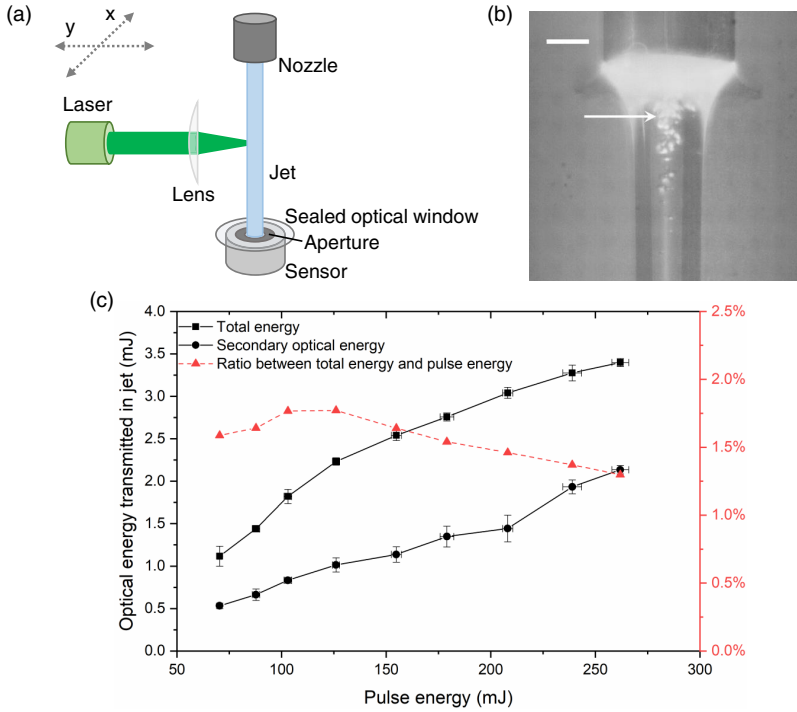


FIG. 8. Measurement of the optical power transmitted in the jet. (a) Experimental setup. Either the 532 nm, 9 ns high-energy pulsed laser or the 520 nm continuous wave (cw) laser are used in this experiment. The laser beam was focused by a convex lens ( $f = 250$  mm, Thorlabs) before the arrival of the DI water microjet of  $160 \mu\text{m}$  in diameter. The jet impinged onto the sensor protected by a sealed optical window made by the  $\sim 100 \mu\text{m}$  transparent polyethylene terephthalate film before breakup, which is covered by an aperture made by a metal plate with a  $\sim 500 \mu\text{m}$  diameter hole to block the unwanted scattered light from the ambient. The water was removed promptly by porous media (not shown) around the window. (b) Bubbles appeared at the nozzle orifice at  $t = 500$  ns after the ablation. The scaling bar is  $100 \mu\text{m}$ , the liquid is DI water, and the laser pulse is 1064 nm, 9 ns, 700 mJ. (c) Transmitted optical energy vs pulse energy when the jet is ablated by the 532 nm high-energy laser.

illuminates the jet, no plasma is produced due to the low-power flux; therefore a simple and ineffective geometric optical coupling is expected. Indeed, the transmitted power is only  $26 \mu\text{W}$ , which corresponds to a coupling efficiency of  $\eta = 3 \times 10^{-5}$ . Such low coupling efficiency suggests that, if the pulsed laser also follows the geometric optical coupling mechanism, for a typical 100 mJ input laser pulse energy, only  $\sim 3 \mu\text{J}$  optical energy can be transmitted within the jet, which is far from enough to cause microexplosions at the nozzle orifice.

When the jet is ablated by the 9 ns, 532 nm laser pulse [Fig. 8(c)], the coupling efficiency jumps to  $\eta \sim 1.8\%$ , suggesting a different coupling mechanism. When the pulse energy is 100 mJ, the optical energy reaching the nozzle orifice is  $E_t \sim 1.75$  mJ. Such energy level and power density can explain how the microexplosion occurs at the nozzle orifice and the nozzle tip damage is observed within 20 blasts. Considering that the transmitted optical energy may consist of energy from both primary pulsed laser irradiation and secondary optical emission (i.e., the plasma flash), we place a notch filter (NF533-17, Thorlabs) that blocks the 532 nm primary laser in front of the energy meter. With the notch filter, the measured energy is only a half of the value without the filter. The result suggests that about half of the optical energy is from the secondary optical emission [see line marked by circular dots in Fig. 8(c)], while another half is from the primary 532 nm laser irradiation.

The plasma generated at the early stage (within a few hundred picoseconds) of the ablation redirects part of the pulsed laser energy into the liquid jet [35–37], resulting in much more efficient optical coupling efficiency than that of a jet irradiated by a cw laser.

A more accurate estimation of the energy density and power density at the nozzle orifice can help to better understand the coupling mechanism. The damage threshold of the stainless steel ablated by laser pulses is influenced by several factors, including laser wavelength, laser pulse duration, and ambient environment (in vacuum or air) [38]. For a  $\sim$ ns or longer laser pulse, the ablation threshold scales with the square root of the pulse duration [39,40]. The damage threshold for stainless steel for a 5 ns pulse is  $\sim 0.2$  J/cm<sup>2</sup> [38]. We can then estimate that for  $\sim 10$  ns and  $\sim 2$   $\mu$ s (the typical duration of the plasma flash) pulses the ablation thresholds in vacuum are about 0.3 and 4 J/cm<sup>2</sup>, respectively. Further, the nonvacuum environment may lead to a decrease of threshold by a factor of 2–3 [38], reducing the thresholds to  $\sim 0.1$  and  $\sim 1.3$  J/cm<sup>2</sup> for  $\sim 10$  ns and  $\sim 2$   $\mu$ s pulses, respectively. In our experiments, deposition of the optical energy at the nozzle orifice occurs at a circular region of  $\sim 300$   $\mu$ m in diameter. The reflectivity of stainless steel varies from  $\sim 10\%$  to  $\sim 70\%$  depending on the light wavelength and surface roughness [41]. For an 800  $\mu$ J pulse (which is a typical value for both primary irradiation and secondary emission when the jet is ablated by a  $\sim 100$  mJ laser pulse), the net deposited energy density ranges from  $\sim 0.1$  to  $\sim 0.8$  J/cm<sup>2</sup>, which is between the damage threshold of the primary irradiation and secondary emission. Therefore, for the phenomenon at the nozzle orifice described in Secs. III A–III C, only the energy density of the coupled primary laser irradiation with  $\sim 10$  ns pulse duration is above the damage threshold. When the liquid is switched to ARI solution, the primary 532 nm irradiation is completely absorbed and only the secondary broadband emission of  $\sim 2$   $\mu$ s from plasma can reach the nozzle tip. This energy is below the damage threshold and is not likely to cause any material removal.

The liquid sheet formation is attributed to a thermally driven phase explosion due to the rapid and localized heating of the liquid. The heat transfer process is the following: The coupled laser optical energy is partially absorbed by the stainless steel and increases the surface temperature of the nozzle orifice, which in turn heats up the water in contact with it. Because of the short duration of the laser pulse ( $\sim 10$  ns), the heat absorbed by the stainless steel only diffuses a short distance into the nozzle material and the water, and thus a strong localized heating becomes possible. To estimate the temperature rise of the stainless steel, we assume that (a) the heating occurs at the stainless-steel interface; (b) the thickness of the heated stainless-steel layer  $\delta_w$  at the end of the laser pulse is given by the thermal diffusion length,  $\delta = (2\alpha\Delta t)^{1/2}$ , where  $\alpha$  is the thermal diffusivity of the stainless steel, and  $\Delta t$  is the laser pulse duration. With  $\alpha \sim 11$  mm<sup>2</sup>/s and  $\sim 10$  ns, we obtained  $\delta \sim 0.5$   $\mu$ m. Considering the annular-shaped nozzle orifice with 310  $\mu$ m outer diameter and 160  $\mu$ m inner diameter, and the energy absorption rate of stainless steel might be only 30%, it is reasonable to assume that about 150  $\mu$ J of energy is absorbed by the thin layer of stainless steel, which instantly heats the thin layer within the nozzle orifice to  $T_s \sim 1600$  K.

Because the heated stainless-steel layer is very thin compared with the nozzle diameter, we apply the model of two infinitely large objects of different temperatures that are suddenly in contact [42] to estimate the temperature of the water-stainless interface ( $T_i$ ) immediately after the laser pulse:

$$T_i = \frac{(k\rho c)_w^{1/2}T_w + (k\rho c)_s^{1/2}T_s}{(k\rho c)_w^{1/2} + (k\rho c)_s^{1/2}}, \quad (3)$$

where  $k$ ,  $\rho$ , and  $c$  are the thermal conductivity, density, and specific heat, respectively (subscript  $w$  refers to the water; subscript  $s$  refers to the stainless steel). For typical material properties:  $k_w = 0.6$  W/(m K),  $\rho_w = 1000$  kg/m<sup>3</sup>,  $c_w = 4200$  J/kg/K,  $k_s \approx 30$  W/(m K),  $\rho_s = 7800$  kg/m<sup>3</sup>,  $c_s = 460$  J/kg/K,  $T_w = 300$  K, and  $T_s = 1600$  K:

$$T_i \approx 1400 \text{ K}, \quad (4)$$

which is much higher than the superheating limit of water of  $\sim 575$  K [43]. Therefore, the absorbed energy is sufficient to heat the thin layer of water beyond the boiling point to induce phase explosion

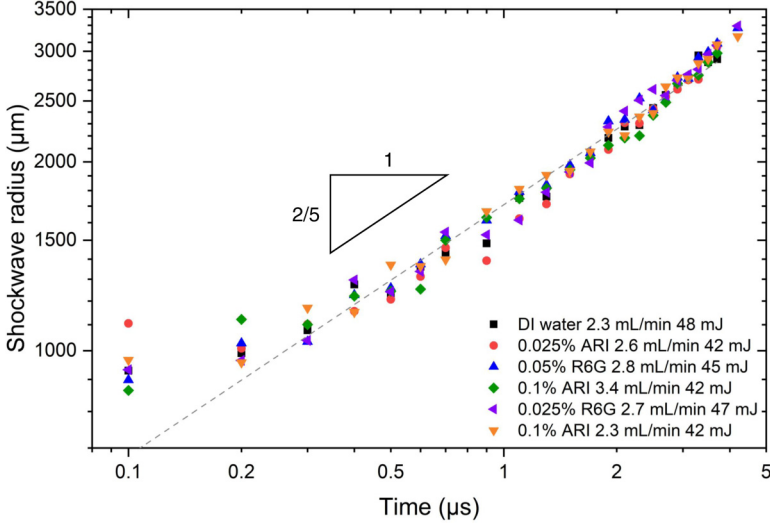


FIG. 9. Shock wave radius vs time. Considering the shape of the shock wave is not a standard sphere, we used the volume of the region behind the shock wave to calculate the effective radius. The dashed line shows the fitting result of the DI water experiment using Taylor's blast model.

that propels liquid away and forms the liquid sheet near the nozzle orifice. This physical picture can also be supported by the bubbles formed several hundred nanoseconds after the ablation while the shock wave generated at the ablation center has not yet reached the nozzle tip [Fig. 8(b)].

### E. Blast energy estimation

The violent blast induced by the laser pulse generates a quasispherical shock wave expanding in the air [Figs. 2 and 9]. The energy deposited can be estimated by Taylor's blast model [44]:

$$E = A \frac{R_s(t)^5 \rho_g}{t^2}, \quad (5)$$

where  $E$  is the energy injected to the blast,  $R_s(t)$  is the radius of the spherical shock wave,  $\rho_g$  is the gas density before the blast,  $t$  is the time interval for the shock to reach  $R_s(t)$ , and  $A$  is a constant close to unity ( $A = 1.03$ , to be exact) [45]. Figure 9 shows the shock wave radius expansion history for jets of different liquids ablated with comparable laser pulse energies. The shock wave radius history is similar for all jets (Fig. 9). The blast energy estimated by Eq. (5) is about 14 mJ, which is 29% of the laser pulse energy. The absorption of a 532 nm laser of  $\sim 100$   $\mu\text{m}$  depth of DI water is only  $10^{-3}$ . The substantial absorption enhancement is through early ionized matter and plasma [46,47]. The liquid with high absorption rate (ARI solution) also shows a similar deposition rate of laser energy, providing evidence of saturation of energy deposition [25].

The shock wave expansion history can also provide information about the temperature and pressure behind the shock wave:

$$\text{Ma} = \frac{V_s}{a_1} = \frac{V_s}{\sqrt{\gamma R_0 T_1}}, \quad (6)$$

$$\frac{P_2}{P_1} = 1 + \frac{2\gamma}{\gamma + 1} (\text{Ma}^2 - 1), \quad (7)$$

$$\frac{T_2}{T_1} = \frac{P_2}{P_1} \left( \frac{\frac{\gamma+1}{\gamma-1} + \frac{P_2}{P_1}}{1 + \frac{\gamma+1}{\gamma-1} \frac{P_2}{P_1}} \right), \quad (8)$$

TABLE I. Temperature and pressure after the shock wave.

Time ( $\mu\text{s}$ )	Temperature (K)	Pressure (bars)
0.25	1064	24.5
0.5	787	10.6
1.0	490	4.3
1.5	398	2.6
2.0	350	1.8
3.0	298	1.1

where  $\text{Ma}$  is the Mach number,  $V_s$  is the velocity of shock wave,  $a_1$  is the sound velocity in surrounding air,  $\gamma$  is the specific heat ratio (for air  $\gamma \approx 1.4$ ),  $R_0$  is the gas constant (for air  $R_0 = 287 \text{ m}^2 \text{ s}^{-2} \text{ K}^{-1}$ ),  $P$  is pressure, and  $T$  is temperature. The subscript 1 denotes the conditions ahead of the shock wave, i.e., in the quiescent air; the subscript 2 denotes the conditions behind the shock wave. Equation (5) can be rewritten as

$$R_s(t) = Kt^{2/5}, \quad (9)$$

where  $K = (E/\rho_g)^{1/5}$  is a constant in a specific experiment that can be obtained by fitting the experimental data. Taking the derivative of Eq. (9) yields

$$V_s = \frac{dR_s(t)}{dt} = \frac{2}{5}Kt^{-3/5}, \quad (10)$$

Hence the pressure behind the expanding shock wave is

$$P_2 = \left\{ 1 + \frac{2\gamma}{\gamma + 1} \left[ \left( \frac{2}{5} \frac{Kt^{-3/5}}{a_1} \right)^2 - 1 \right] \right\} P_1. \quad (11)$$

Similarly, the temperature can be estimated. Table I shows the temperature and pressure history. Several hundreds of nanoseconds after the blast, the temperature can reach over 1000 K, and the pressure can be more than 20 times atmospheric pressure behind the shock wave. Both values decay rapidly: Within 3  $\mu\text{s}$ , or 2.5 mm radius, the temperature drops from >1000 K to nearly room temperature (298 K), and the pressure drops from 24 bars to merely 10% above atmosphere pressure. The rapid drop in both pressure and temperature suggests the blast only affects a limited zone of a few millimeters.

#### IV. CONCLUSION

A microjet of  $\sim 100$  micrometers in radius subject to ablation of an intense nanosecond laser pulse (power flux of  $10^{13}$ – $10^{14} \text{ W/m}^2$  in this work) breaks into two liquid columns. The gap between the two liquid columns expands with respect to time, and the logarithm scaling of gap expansion, originally derived from microjets of several micrometers in diameter ablated by a femtosecond x-ray laser, also applied to our experiments ( $\sim 160 \mu\text{m}$  diameter jet ablated by nanosecond 532 and 1064 nm laser pulse). The shock wave generated from the blast expands in the surrounding air, from which the effective blast energy can be estimated. When the liquid is transparent to the laser pulse,  $\sim 3.5\%$  of the laser pulse energy can enter the jet and half can reach the nozzle orifice as far as 50 times the jet diameter away from the blast center through internal reflections. The energy density absorbed by the nozzle orifice exceeds the damage threshold of stainless steel, causing microexplosions and formation of a liquid sheet near the nozzle orifice. The detailed mechanism of plasma generation and its scattering of optical energy is a subject of future investigation.

Previous works [24–26, 48–50] have shown that the *mechanical* effect (i.e., the shock wave) that originated from the blast center could propagate along the jets for more than ten times the jet radius.

This study expands that physical picture by showing the *optical* effect: The optical energy can transmit for a relatively long distance through the internal reflection within a liquid jet ablated by an intense laser pulse. The short optical energy pulse deposited on the absorptive nozzle surface can lead to enormous power flux, tightly localized heating, and a microexplosion that expels the liquid to form an expanding sheet. The optical energy pulse from the XFEL induced plasma may also instantly heat up the absorbing samples carried by the jet for SFX applications. Another possible application could be the water jet guided laser machining [51]: The micro-water-jet can be used as a waveguide to deliver the pulsed energy for places hard to reach by a focused laser. The liquid jet can also provide cooling simultaneously to reduce the heat affected zone (HAZ).

#### ACKNOWLEDGMENT

W.D. acknowledges the financial support from the National Science Foundation of China (Grants No. 11932009 and No. 11872199).

- 
- [1] A. Vogel, N. Linz, S. Freidank, and G. Paltauf, Femtosecond-Laser-Induced Nanocavitation in Water: Implications for Optical Breakdown Threshold and Cell Surgery, *Phys. Rev. Lett.* **100**, 038102 (2008).
  - [2] A. Vogel, S. Busch, and U. Parlitz, Shock wave emission and cavitation bubble generation by picosecond and nanosecond optical breakdown in water, *J. Acoust. Soc. Am.* **100**, 148 (1996).
  - [3] C. B. Schaffer, N. Nishimura, E. N. Glezer, A. M. T. Kim, and E. Mazur, Dynamics of femtosecond laser-induced breakdown in water from femtoseconds to microseconds, *Opt. Express* **10**, 196 (2002).
  - [4] K. Sokolowski-Tinten, J. Biakowski, A. Cavalleri, D. von der Linde, A. Oparin, J. Meyer-ter-Vehn, and S. I. Anisimov, Transient States of Matter During Short Pulse Laser Ablation, *Phys. Rev. Lett.* **81**, 224 (1998).
  - [5] J. Hermens, H. Gelderblom, B. Liu, J. Duffhues, P. Rindt, and O. O. Versolato, Laser-impact-induced splashing: An analysis of the splash crown evolution after Nd:YAG ns-pulse laser impact on a liquid tin pool, *Appl. Phys. B: Lasers Opt.* **127**, 44 (2021).
  - [6] S. R. G. Avila and C. D. Ohl, Fragmentation of acoustically levitating droplets by laser-induced cavitation bubbles, *J. Fluid Mech.* **805**, 551 (2016).
  - [7] D. Keefe, Inertial confinement fusion, *Annu. Rev. Nucl. Part. Sci.* **32**, 391 (1982).
  - [8] C. Wagner and N. Harned, EUV lithography: Lithography gets extreme, *Nat. Photonics* **4**, 24 (2010).
  - [9] H. N. Chapman, P. Fromme, A. Barty, T. A. White, R. A. Kirian, A. Aquila, M. S. Hunter, J. Schulz, D. P. DePonte, U. Weierstall, R. B. Doak, F. R. N. C. Maia, A. V. Martin, I. Schlichting, L. Lomb, N. Coppola, R. L. Shoeman, S. W. Epp, R. Hartmann, D. Rolles *et al.*, Femtosecond X-ray protein nanocrystallography, *Nature (London)* **470**, 73 (2011).
  - [10] S. Boutet, L. Lomb, G. J. Williams, T. R. M. Barends, A. Aquila, R. B. Doak, U. Weierstall, D. P. DePonte, J. Steinbrener, R. L. Shoeman, M. Messerschmidt, A. Barty, T. A. White, S. Kassemeyer, R. A. Kirian, M. M. Seibert, P. A. Montanez, C. Kenney, R. Herbst, P. Hart *et al.*, High-resolution protein structure determination by serial femtosecond crystallography, *Science* **337**, 362 (2012).
  - [11] K. M. George, J. T. Morrison, S. Feister, G. K. Ngirmang, J. R. Smith, A. J. Klim, J. Snyder, D. Austin, W. Erbsen, K. D. Frische, J. Nees, C. Orban, E. A. Chowdhury, and W. M. Roquemore, High-repetition-rate ( $\geq$ kHz) targets and optics from liquid microjets for high-intensity laser-plasma interactions, *High Power Laser Sci Eng.* **7**, 03000e50 (2019).
  - [12] Y. Glinec, J. Faure, L. L. Dain, S. Darbon, T. Hosokai, J. J. Santos, E. Lefebvre, J. P. Rousseau, F. Burgy, B. Mercier, and V. Malka, High-Resolution  $\gamma$ -Ray Radiography Produced by a Laser-Plasma Driven Electron Source, *Phys. Rev. Lett.* **94**, 025003 (2005).
  - [13] M. Borghesi, A. J. Mackinnon, D. H. Campbell, D. G. Hicks, S. Kar, P. K. Patel, D. Price, L. Romagnani, A. Schiavi, and O. Willi, Multi-MeV Proton Source Investigations in Ultraintense Laser-Foil Interactions, *Phys. Rev. Lett.* **92**, 055003 (2004).

- [14] M. M. Murnane, H. C. Kapteyn, M. D. Rosen, and R. W. Falcone, Ultrafast x-ray pulses from laser-produced plasmas, *Science* **251**, 531 (1991).
- [15] S. V. Bulanov, T. Z. Esirkepov, V. S. Khoroshkov, A. V. Kunetsov, and F. Pegoraro, Oncological hadrontherapy with laser ion accelerators, *Phys. Lett. A* **299**, 240 (2002).
- [16] L. Disdier, J. P. Garçonnet, G. Malka, and J. L. Miquel, Fast Neutron Emission from a High-Energy Ion Beam Produced by a High-Intensity Subpicosecond Laser Pulse, *Phys. Rev. Lett.* **82**, 1454 (1999).
- [17] S. Mondal, M. Shirozhan, N. Ahmed, M. Bocoum, F. Boehle, A. Vernier, S. Haessler, R. Lopez-Martens, F. Sylla, C. Sire, F. Quere, K. Nelissen, K. Varju, D. Charalambidis, and S. Kahaly, Surface plasma attosource beamlines at ELI-ALPS, *J. Opt. Soc. Am. B* **35**, A93 (2018).
- [18] C. Danson, D. Hillier, N. Hopps, and D. Neely, Petawatt class lasers worldwide, *High Power Laser Sci. Eng.* **3**, e3 (2015).
- [19] I. Prencipe, J. Fuchs, S. Pascarelli, D. W. Schumacher, R. B. Stephens, N. B. Alexander, R. Briggs, M. Buescher, M. O. Cernaianu, A. Choukourou, M. De Marco, A. Erbe, J. Fassbender, G. Fiquet, P. Fitzsimmons, C. Gheorghiu, J. Hund, L. G. Huang, M. Harmand, N. J. Hartley *et al.*, Targets for high repetition rate laser facilities: Needs, challenges and perspectives, *High Power Laser Sci. Eng.* **5**, e17 (2017).
- [20] R. Neutze, G. Branden, and G. F. X. Schertler, Membrane protein structural biology using x-ray free electron lasers, *Curr. Opin. Struct. Biol.* **33**, 115 (2015).
- [21] P. Emma, R. Akre, J. Arthur, R. Bionta, C. Bostedt, J. Bozek, A. Brachmann, P. Bucksbaum, R. Coffee, F. J. Decker, Y. Ding, D. Dowell, S. Edstrom, A. Fisher, J. Frisch, S. Gilevich, J. Hastings, G. Hays, P. Hering, Z. Huang *et al.*, First lasing and operation of an angstrom-wavelength free-electron laser, *Nat. Photonics* **4**, 641 (2010).
- [22] K. Ueda, X-ray free-electron laser, *Appl. Sci.* **8**, 879 (2018).
- [23] S. Pandey, R. Bean, T. Sato, I. Poudyal, J. Bielecki, J. Cruz Villarreal, O. Yefanov, V. Mariani, T. A. White, C. Kupitz, M. Hunter, M. H. Abdellatif, S. Bajt, V. Bondar, A. Echelmeier, D. Doppler, M. Emons, M. Frank, R. Fromme, Y. Gevorkov *et al.*, Time-resolved serial femtosecond crystallography at the European XFEL, *Nat. Methods* **17**, 73 (2020).
- [24] C. A. Stan, D. Milathianaki, H. Laksmono, R. G. Sierra, T. A. McQueen, M. Messerschmidt, G. J. Williams, J. E. Koglin, T. J. Lane, M. J. Hayes, S. A. H. Guillet, M. N. Liang, A. L. Aquila, P. R. Willmott, J. S. Robinson, K. L. Gumerlock, S. Botha, K. Nass, I. Schlichting, R. L. Shoeman *et al.*, Liquid explosions induced by x-ray laser pulses, *Nat. Phys.* **12**, 966 (2016).
- [25] D. Ursescu, V. Aleksandrov, D. Matei, I. Dancus, M. D. de Almeida, and C. A. Stan, Generation of shock trains in free liquid jets with a nanosecond green laser, *Phys. Rev. Fluids* **5**, 123402 (2020).
- [26] G. Blaj, M. N. Liang, A. L. Aquila, P. R. Willmott, J. E. Koglin, R. G. Sierra, J. S. Robinson, S. Boutet, and C. A. Stan, Generation of high-intensity ultrasound through shock propagation in liquid jets, *Phys. Rev. Fluids* **4**, 043401 (2019).
- [27] S. Tait, E. T. White, and J. D. Litster, Mechanical characterization of protein crystals, *Part. Part. Syst. Charact.* **25**, 266 (2008).
- [28] H. Koizumi, H. Kawamoto, M. Tachibana, and K. Kojima, Effect of intracrystalline water on micro-Vickers hardness in tetragonal hen egg-white lysozyme single crystals, *J. Phys. D: Appl. Phys.* **41**, 074019 (2008).
- [29] A. L. Klein, W. Bouwhuis, C. W. Visser, H. Lhuissier, C. Sun, J. H. Snoeijer, E. Villermaux, D. Lohse, and H. Gelderblom, Drop Shaping by Laser-Pulse Impact, *Phys. Rev. Appl.* **3**, 044018 (2015).
- [30] A. Penzkofer and W. Leupacher, Fluorescence behavior of highly concentrated rhodamine 6G solutions, *J. Lumin.* **37**, 61 (1987).
- [31] H. Gelderblom, H. Lhuissier, A. L. Klein, W. Bouwhuis, D. Lohse, E. Villermaux, and J. H. Snoeijer, Drop deformation by laser-pulse impact, *J. Fluid Mech.* **794**, 676 (2016).
- [32] A. L. Klein, D. Kurilovich, H. Lhuissier, O. O. Versolato, D. Lohse, E. Villermaux, and H. Gelderblom, Drop fragmentation by laser-pulse impact, *J. Fluid Mech.* **893**, A7 (2020).
- [33] A. L. Klein, C. W. Visser, W. Bouwhuis, H. Lhuissier, C. Sun, J. H. Snoeijer, E. Villermaux, D. Lohse, and H. Gelderblom, Laser impact on a drop, *Phys. Fluids* **27**, 091106 (2015).

- [34] See Supplemental Material at <http://link.aps.org/supplemental/10.1103/PhysRevFluids.7.034001> for additional movies showing the laser blast phenomena over a comprehensive range of conditions.
- [35] D. Panasenکو, A. J. Shu, A. Gonsalves, K. Nakamura, N. H. Matlis, C. Toth, and W. P. Leemans, Demonstration of a plasma mirror based on a laminar flow water film, *J. Appl. Phys.* **108**, 044913 (2010).
- [36] C. K. Li, F. H. Séguin, J. A. Frenje, J. R. Rygg, R. D. Petrasso, R. P. J. Town, P. A. Amendt, S. P. Hatchett, O. L. Landen, A. J. Mackinnon, P. K. Patel, M. Tabak, J. P. Knauer, T. C. Sangster, and V. A. Smalyuk, Observation of the Decay Dynamics and Instabilities of Megagauss Field Structures in Laser-Produced Plasmas, *Phys. Rev. Lett.* **99**, 015001 (2007).
- [37] D. Devaux, R. Fabbro, L. Tollier, and E. Bartnicki, Generation of shock waves by laser-induced plasma in confined geometry, *J. Appl. Phys.* **74**, 2268 (1993).
- [38] M. Wisse, L. Marot, B. Eren, R. Steiner, D. Mathys, and E. Meyer, Laser damage thresholds of ITER mirror materials and first results on *in situ* laser cleaning of stainless steel mirrors, *Fusion Eng. Des.* **88**, 388 (2013).
- [39] E. G. Gamaly, A. V. Rode, B. Luther-Davies, and V. T. Tikhonchuk, Ablation of solids by femtosecond lasers: Ablation mechanism and ablation thresholds for metals and dielectrics, *Phys. Plasmas* **9**, 949 (2002).
- [40] M. D. Shirk and P. A. Molian, A review of ultrashort pulsed laser ablation of materials, *J. Laser Appl.* **10**, 18 (1998).
- [41] Y. Namba, Specular spectral reflectance of A1S1304 stainless steel at near-normal incidence, in *26th Annual Technical Symposium* (SPIE, Bellingham, WA, 1983), p. 93.
- [42] F. Incropera and D. Dewitt, *Fundamentals of Heat and Mass Transfer*, 4th ed. (Wiley, New York, 2011).
- [43] C. T. Avedisian, The homogeneous nucleation limits of liquids, *J. Phys. Chem. Ref. Data* **14**, 695 (1985).
- [44] G. Taylor, The formation of a blast wave by a very intense explosion. II. The atomic explosion of 1945, *Proc. R. Soc. London, Ser. A* **201**, 175 (1950).
- [45] B. Lautrup, *Physics of Continuous Matter: Exotic and Everyday Phenomena in the Macroscopic World*, 2nd ed. (CRC Press, Boca Raton, FL, 2011).
- [46] C. V. Bindhu, S. S. Harilal, M. S. Tillack, F. Najmabadi, and A. C. Gaeris, Energy absorption and propagation in laser-created sparks, *Appl. Spectrosc.* **58**, 719 (2004).
- [47] C. V. Bindhu, S. S. Harilal, M. S. Tillack, F. Najmabadi, and A. C. Gaeris, Laser propagation and energy absorption by an argon spark, *J. Appl. Phys.* **94**, 7402 (2003).
- [48] E. Villermaux and B. Bossa, Drop fragmentation on impact, *J. Fluid Mech.* **668**, 412 (2011).
- [49] E. Villermaux and C. Clanet, Life of a flapping liquid sheet, *J. Fluid Mech.* **462**, 341 (2002).
- [50] C. Clanet and E. Villermaux, Life of a smooth liquid sheet, *J. Fluid Mech.* **462**, 307 (2002).
- [51] Y. Liu, M. Wei, T. Zhang, H. Qiao, and H. Li, Overview on the development and critical issues of water jet guided laser machining technology, *Opt. Laser Technol.* **137**, 106820 (2021).